Backscattering position detection for photonic force microscopy

Giovanni Volpe[a)]
ICFO—Institut de Ciencies Fotoniques, Mediterranean Technology Park, Castelldefels, Barcelona, 08860 Spain

Gregory Kozyreff[b)]
Optique Nonlinéaire Théorique, Université Libre de Bruxelles (U.L.B.), Code Postal 231, Campus Plaine, B-1050 Bruxelles, Belgium and ICFO—Institut de Ciencies Fotoniques, Mediterranean Technology Park, Castelldefels, Barcelona, 08860 Spain

Dmitri Petrov[c)]
ICFO—Institut de Ciencies Fotoniques, Mediterranean Technology Park, Castelldefels, Barcelona, 08860 Spain and ICREA—Institució Catalana de Recerca i Estudis Avançats, Barcelona, 08010 Spain

(Received 3 June 2007; accepted 25 August 2007; published online 23 October 2007)

An optically trapped particle is an extremely sensitive probe for the measurement of pico- and femto-Newton forces between the particle and its environment in microscopic systems (photonic force microscopy). A typical setup comprises an optical trap, which holds the probe, and a position sensing system, which uses the scattering of a beam illuminating the probe. Usually the position is accurately determined by measuring the deflection of the forward-scattered light transmitted through the probe. However, geometrical constraints may prevent access to this side of the trap, forcing one to make use of the backscattered light instead. A theory is presented together with numerical results that describes the use of the backscattered light for position detection. With a Mie–Debye approach, we compute the total (incident plus scattered) field and follow its evolution as it is collected by the condenser lenses and projected onto the position detectors and the responses of position sensitive detectors and quadrant photodetectors to the displacement of the probe in the optical trap, both in forward and backward configurations. We find out that in the case of backward detection, for both types of detectors the displacement sensitivity can change sign as a function of the probe size and is null for some critical sizes. In addition, we study the influence of the numerical aperture of the detection system, polarization, and the cross talk between position measurements in orthogonal directions. We finally discuss how these features should be taken into account in experimental designs. © *2007 American Institute of Physics*. [DOI: 10.1063/1.2799047]

I. INTRODUCTION

The detection and measurement of forces and torques in microscopic systems is an important goal in many areas such as biophysics, colloidal physics, and hydrodynamics of small systems. Since 1993, the photonic force microscopy (PFM) has become an important tool to probe forces in microscopic systems.[1,2] A typical PFM setup comprises an optical trap that holds a probe—a dielectric or metallic particle of micrometer size—and a position sensing system. In the case of biophysical applications the probe is a small latex bead tethered to the cell or molecule under study. The probe randomly moves due to Brownian motion in the potential well formed by the optical trap. Near the center of the trap, the optical trapping potential is parabolic and the restoring force is linear in the displacement. The restoring force of the optical trap in each direction may be deduced from the three-dimensional position fluctuation spectrum. After this calibration procedure, the measurement of an external force is now reduced to the measurement of the position of the probe in the range where the parabolic approximation is valid.

The three-dimensional position of the probe can be measured through the scattering of an auxiliary beam that illuminates the trapped probe. If the intensity of this beam is weak enough not to significantly affect the stiffness of the trap, trapping and detection are independent operations. These conditions are easily achievable and exciting experiments have been realized with such a configuration (for example, see Refs. 3–6).

Let us suppose that the trapping force is linear in the probe displacement over the range of interest, so that any nonlinear response of the PFM can be attributed to the position detection system only. Two crucial parameters of the position detection system are then:

(1) the displacement sensitivity (in V μm^{-1}) and
(2) the linear response range of the position detection system.

Both parameters depend on the intensity distribution that reaches the detector.

Typically, position detection is achieved through the analysis of the interference of the forward-scattered light (FS) and unscattered (incident) light (Fig. 1). The PFM with FS detection was extensively studied, for example, in Refs. 7–17. The importance of this technique is demonstrated by

[a)]Electronic mail: giovanni.volpe@icfo.es
[b)]Electronic mail: gregory.kozyreff@ulb.ac.be
[c)]Electronic mail: dmitri.petrov@icfo.es

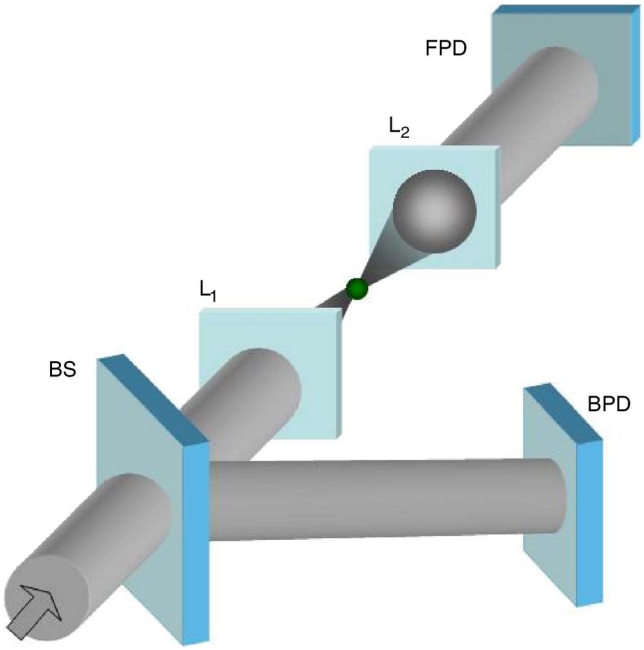

FIG. 1. (Color online) Position detection system for PFM. The detection beam is focused by the lens L_1 on the trapped probe. The interference pattern arising due to the incoming beam and scattered wave can be analyzed by collecting either the forward scattering light with the lens L_2 and measuring the response of the FPD or collecting the backscattering light with the lens L_1 and measuring the response of the BPD.

its exciting applications, for example, in biophysics,[3–6,18] thermodynamics of small systems,[19] and colloidal physics.[20] Recently, subangstrom sensitivity was achieved using a double beam optical trap[21,22] that allows one to measure forces in the femto-Newton range. Furthermore, a careful statistical analysis of the Brownian fluctuations of an optically trapped probe can also reveal the presence of torque acting on it:[23] this method achieves higher torque sensitivity than other techniques and could be applied to the study of proteins and DNA.

Two types of photodetectors are typically used as position sensor. The quadrant photoetector (QPD) works by measuring the intensity difference between the left-right and top-bottom sides of the detection plane. The position sensing detector (PSD) measures the position of the centroid of the collected intensity distribution, giving a more adequate response for non-Gaussian profiles. Note that video systems have also been used, but they cannot achieve the rate of data acquisition available with position photodetectors.[24,25]

However, the FS position detection scheme is not always possible. In a number of experiments, geometrical constraints may prevent access to the FS light, forcing one to make use of the backscattered (BS) light instead (Fig. 1). This occurs, for example, in biophysical applications where one of the two faces of a sample holder needs to be coated with some specific material[26] or in plasmonics applications where a plasmon wave needs to be coupled to one of the faces of the holder.[28] Furthermore, the BS mode of operation makes it easier to combine the optical trap with other techniques such as atomic force microscopy, which requires access to one side of the holder. A special feature of the BS detection compared to the FS case is that the same lens is used both for trapping and for collecting the scattering light. In the literature, the use of the BS light for position and force detection is mentioned[26–31] but, contrary to the FS light detection, has not been discussed extensively.

A remarkable experimental observation in Ref. 31 was that the detection efficiency can significantly depend on the type of detector used when using BS light. In particular, with the experimental parameters cited in Ref. 31, the linear detection range of the PSD was found to be twice that of the QPD for a 2.5-μm probe. This is quite different from the FS setup, where no significant difference was found between both detectors. In addition, the data shown in Ref. 31 indicate that the displacement sensitivity depends on the probe size and even changes sign for small probes. This suggests that for some intermediate probe sizes, the deflection sensitivity should vanish, thus making the PFM inoperative.

Additional issues related to the use of BS light arise when studying forces near surfaces, especially metal ones when reflected waves from the surface affect the position measurements.[28,32]

These observations motivate us to pursue a better theoretical understanding of the possibilities and limitations of the BS position detection in the PFM, as it has already been done for the FS case. Using a Mie–Debye approach similar to Refs. 13, 33, and 34, we compute the electromagnetic field scattered by a spherical trapped probe as a function of probe position, probe size, and numerical aperture of the detection system. We then compute the total field and follow its evolution as it is collected by the condenser lenses and projected onto the position detectors in both the FS and BS configurations. We find that the displacement sensitivity can change its sign, and therefore passes by zero, consistently with the experimental results.[31] Our simulations show that the changes of the sign occur repeatedly as the size is further varied. Qualitatively similar results are obtained by varying the numerical aperture of the lens. This should be taken into account in experimental designs.

II. OPTICAL MODEL OF THE DETECTION SYSTEM

Suppose that the detection beam is focused by an aplanatic lens L_1 which produces a convergent, spherical wave (Fig. 2). The wave propagates to a diffraction-limited axial image. The aperture of the lens R is the entrance pupil of the optical system. Let $\mathbf{b}$ be a vector which describes the position of the probe relative to the focal point. $\mathbf{b}$ is determined only by the trapping beam of the PFM and by the external forces acting on the probe, but it does not depend on the detection beam, which is assumed weak enough not to perturb the equilibrium position of the probe. A condenser lens L_2 (Fig. 1) collects the incident and forward scattering fields onto a forward position detector FPD, which is located at a plane conjugated to the backfocal plane of the condenser lens. The BS field is collected by the lens L_1 and the image on the backfocal plane is transferred by a beamsplitter BS on a back position detector BPD, which is placed in a plane conjugated to the backfocal plane.

The main steps to compute the position detectors response are:

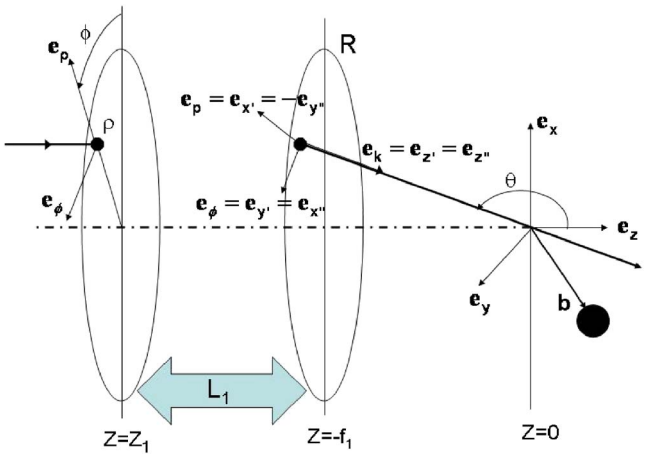

FIG. 2. (Color online) Optical model and reference systems.

(a) to calculate the distribution of the detection field near the focus of the lens L_1;
(b) to solve the corresponding Mie–Debye problem, i.e., to find the scattered wave for each partial plane wave describing the focused field for an arbitrary position of the probe;
(c) to find the total scattered wave and propagate the total field at the backfocal plane of the condenser lens L_2 (the FW detection) or L_1 (the BS detection); and
(d) to calculate the response of the forward position detector (FPD) and BPD in two cases, namely for the QPD and PSD systems.

In what follows we consider the main steps in details.

A. Detection field near the focus of the lens L_1

Assuming paraxial approximation to hold well for the incoming wave $\mathbf{E_i}$, at the entrance plane of the lens L_1 (Fig. 2) we have

$$\mathbf{E_i} = E_\rho(\rho_i, \phi_i)\mathbf{e}_\rho + E_\phi(\rho_i, \phi_i)\mathbf{e}_\phi, \tag{1}$$

where

$$\mathbf{e}_\rho = \cos\ \phi_i \mathbf{e}_x + \sin\ \phi_i \mathbf{e}_y, \tag{2}$$

$$\mathbf{e}_\phi = -\sin\ \phi_i \mathbf{e}_x + \cos\ \phi_i \mathbf{e}_y, \tag{3}$$

and $(\mathbf{e}_x, \mathbf{e}_y, \mathbf{e}_z)$ are the unit vectors of a cartesian coordinate system centered at the focus of L_1. The $\mathbf{e}_\rho$ component corresponds to a p-wave incidence, while the $\mathbf{e}_\phi$ component is a s wave for the focusing lens. Following Ref. 35, we assume that paraxial rays impinging on the lens at a radius ρ_i is deflected with an angle θ_i with respect to the z axis according to

$$\frac{\sin\ \theta_i}{\mathrm{NA}_1/n_m} = \frac{\rho_i}{R}, \tag{4}$$

where NA_1 is the numerical aperture of the lens L_1, n_m is the refraction index outside the lens, and R is the aperture stop radius. This follows from Abbe's sine condition for sharp imaging.[36] Upon deflection toward the focus of the lens, the orientation of the $\mathbf{e}_\phi$ component remains the same, while the $\mathbf{e}_\rho$ component is transformed as

$$\mathbf{e}_p = \cos\ \theta_i \mathbf{e}_\rho + \sin\ \theta_i \mathbf{e}_z. \tag{5}$$

The wave vector of the rays becomes parallel to

$$\mathbf{e}_k = -\sin\ \theta_i \mathbf{e}_\rho + \cos\ \theta_i \mathbf{e}_z. \tag{6}$$

At a point $\mathbf{x}$ near the focus, the incoming field is thus[37]

$$\frac{-if_1}{\lambda}\iint (E_\rho \mathbf{e}_p + E_\phi \mathbf{e}_\phi) e^{i\mathbf{k}_i\cdot\mathbf{x}} \sin\ \theta_i d\theta_i d\phi_i, \tag{7}$$

where f_1 is the focal length of L_1 and λ is the wavelength. Here, $\mathbf{k}_i = k\mathbf{e}_k$, where $k = n_m k_0$ and k_0 is the wave number in vacuum. Using Eq. (4), we express the electric field near the focus of L_1 as an integral over the plane vector waves

$$\frac{-if_1}{\lambda}\left(\frac{\mathrm{NA}_1}{Rn_m}\right)^2 \int_0^R \int_0^{2\pi} (E_\rho \mathbf{e}_p + E_\phi \mathbf{e}_\phi) e^{i\mathbf{k}_i\cdot\mathbf{x}} \frac{\rho_i d\phi_i d\rho_i}{\cos\ \theta_i}. \tag{8}$$

Comparing Eq. (8) with Eq. (2.18) of Ref. 37, we see that Eq. (4) is equivalent to assume no aberration in L_1.

B. Scattering from a spherical particle

We first derive an expression for the scattered field when the probe is located at the focus of L_1 (i.e., $\mathbf{b}=0$). Next, we deduce the corresponding expression for arbitrary $\mathbf{b}$.

1. Sphere at the focus

As Eq. (8) illustrates, the incoming field can be viewed as a superposition of plane waves that are linearly polarized in the $\mathbf{e}_p$ and $\mathbf{e}_\phi$ directions. Using the standard Mie theory[38] in suitably rotated reference frames for each of these plane waves, we find the scattered field $\mathbf{E}_s$. For completeness, we recall the expression of $\mathbf{E}_s$ in Appendix A.

Let us consider first the incident p wave that exits the front principal plane of L_1 at (ρ_i, ϕ_i). Its amplitude is $E_\rho(\rho_i, \phi_i)$ and it is polarized along $\mathbf{e}_{x'}$ in the reference frame $(\mathbf{e}_{x'}, \mathbf{e}_{y'}, \mathbf{e}_{z'}) = (\mathbf{e}_p, \mathbf{e}_\phi, \mathbf{e}_k)$. This wave generates a partial scattered field

$$\begin{aligned} E_\rho(\rho_i, \phi_i)\mathbf{E}_s' &= E_\rho(\rho_i, \phi_i)[E_{s,x}(x', y', z')\mathbf{e}_{x'} \\ &\quad + E_{s,y}(x', y', z')\mathbf{e}_{y'} + E_{s,z}(x', y', z')\mathbf{e}_{z'}] \\ &= E_\rho(\rho_i, \phi_i)\sum_j E_{s,j}(\mathbf{x}')\mathbf{e}_j', \end{aligned} \tag{9}$$

where the functions $E_{s,x}(x,y,z)$, $E_{s,y}(x,y,z)$, and $E_{s,z}(x,y,z)$ are the cartesian components of the scattered field produced by a plane wave that is polarized in the x direction and propagating in the z direction, as given in Ref. 38. On the other hand, the coordinates $\mathbf{x}' = (x', y', z')$ are relative to the $(\mathbf{e}_{x'}, \mathbf{e}_{y'}, \mathbf{e}_{z'})$ frame.

Similarly, the $E_\phi(\rho_i, \phi_i)$ amplitude is associated to an $\mathbf{e}_{x''}$-polarized wave in the reference frame $(\mathbf{e}_{x''}, \mathbf{e}_{y''}, \mathbf{e}_{z''}) = (\mathbf{e}_\phi, -\mathbf{e}_p, \mathbf{e}_k)$ and leads to the partial scattered field

$$E_\phi(\rho_i, \phi_i)\mathbf{E}_s'' = E_\phi(\rho_i, \phi_i)\sum_j E_{s,j}(\mathbf{x}'')\mathbf{e}_j''. \tag{10}$$

The total scattered field is, therefore, given by

$$\frac{-if_1}{\lambda}\left(\frac{NA_1}{Rn_m}\right)^2\iint [E_\rho(\rho_i,\phi_i)\mathbf{E}_s' + E_\phi(\rho_i,\phi_i)\mathbf{E}_s'']\frac{\rho_i d\rho_i d\phi_i}{\cos\theta_i}. \tag{11}$$

To compute this integral, we need to relate the coordinates (x,y,z), (x',y',z'), and (x'',y'',z'') of a given vector in the three coordinate systems. We find (Appendix B) that

$$\begin{pmatrix} x \\ y \\ z \end{pmatrix} = \mathsf{M}_\rho \begin{pmatrix} x' \\ y' \\ z' \end{pmatrix} = \mathsf{M}_\phi \begin{pmatrix} x'' \\ y'' \\ z'' \end{pmatrix}, \tag{12}$$

where the rotation matrices M_ρ and M_ϕ are given by

$$\mathsf{M}_\rho = \begin{pmatrix} \cos\theta_i\cos\phi_i & -\sin\phi_i & -\cos\phi_i\sin\theta_i \\ \cos\theta_i\sin\phi_i & \cos\theta_i & -\sin\theta_i\sin\phi_i \\ \sin\theta_i & 0 & \cos\theta_i \end{pmatrix},$$

$$\mathsf{M}_\phi = \begin{pmatrix} -\sin\phi_i & -\cos\theta_i\cos\phi_i & -\cos\phi_i\sin\theta_i \\ \cos\phi_i & -\cos\theta_i\sin\phi_i & -\sin\theta_i\sin\phi_i \\ 0 & -\sin\theta_i & \cos\theta_i \end{pmatrix}. \tag{13}$$

Hence, combining Eqs. (9)–(12), the total scattered field (11) is

$$\mathbf{E}_{s,\mathrm{tot}}(\mathbf{x}) = \frac{-if_1}{\lambda}\left(\frac{NA_1}{Rn_m}\right)^2\iint [E_\rho(\rho_i,\phi_i)\mathsf{M}_\rho\mathbf{E}_s(\mathsf{M}_\rho^{-1}\mathbf{x}) + E_\phi(\rho_i,\phi_i)\mathsf{M}_\phi\mathbf{E}_s(\mathsf{M}_\phi^{-1}\mathbf{x})]\frac{\rho_i d\rho_i d\phi_i}{\cos\theta_i}. \tag{14}$$

2. Sphere out of the focus

Using Eq. (14), we can now express the scattered field for the sphere away from the focus ($\mathbf{b}\neq 0$). We first note from Eq. (8) that the incoming field is now dephased by an amount $\exp(i\mathbf{k}_i\cdot\mathbf{b})$. Second, the origin of the scattered field is now shifted to the probe position. We thus have to apply the transformations

$$E_{\rho,\phi}(\rho_i,\phi_i) \to E_{\rho,\phi}(\rho_i,\phi_i)e^{i\mathbf{k}_i\cdot\mathbf{b}}, \tag{15}$$

$$\mathbf{E}_s(\mathsf{M}_{\rho,\phi}^{-1}\mathbf{x}) \to \mathbf{E}_s[\mathsf{M}_{\rho,\phi}^{-1}(\mathbf{x}-\mathbf{b})], \tag{16}$$

and the expression for the total scattered field becomes

$$\mathbf{E}_{s,\mathrm{tot}} = \frac{-if_1}{\lambda}\left(\frac{NA_1}{Rn_m}\right)^2\iint \{E_\rho(\rho_i,\phi_i)\mathsf{M}_\rho\mathbf{E}_s[\mathsf{M}_\rho^{-1}(\mathbf{x}-\mathbf{b})] + E_\phi(\rho_i,\phi_i)\mathsf{M}_\phi\mathbf{E}_s[\mathbf{M}_\phi^{-1}(\mathbf{x}-\mathbf{b})]\}e^{i\mathbf{k}_i\cdot\mathbf{b}}\frac{\rho_i d\rho_i d\phi_i}{\cos\theta_i}. \tag{17}$$

Furthermore, simplifications can be made at distances $|\mathbf{x}|$ large compared to $|\mathbf{b}|$ and to the wavelength. On the one hand, we note that the angular dependence of $\mathbf{E}_s[\mathsf{M}_\phi^{-1}(\mathbf{x}-\mathbf{b})]$ differs only from that of $\mathbf{E}_s(\mathsf{M}_\phi^{-1}\mathbf{x})$ by an $O(|\mathbf{b}|/|\mathbf{x}|)$ quantity. On the other hand, the radial dependence of $\mathbf{E}_s$ is controlled asymptotically by a phase factor

$$\frac{e^{ik|\mathbf{x}-\mathbf{b}|}}{k|\mathbf{x}-\mathbf{b}|} \sim \frac{e^{ik|\mathbf{x}|}}{k|\mathbf{x}|}e^{-ik\mathbf{x}\cdot\mathbf{b}/|\mathbf{x}|}, \tag{18}$$

when $k|\mathbf{x}|\gg 1$. Hence, we obtain

$$\mathbf{E}_{s,\mathrm{tot}}(\mathbf{x}) \sim \frac{-if_1}{\lambda}\left(\frac{NA_1}{Rn_m}\right)^2 e^{-ik(\mathbf{x}\cdot\mathbf{b}/|\mathbf{x}|)}\iint [E_\rho(\rho_i,\phi_i)\mathsf{M}_\rho\mathbf{E}_s(\mathsf{M}_\rho^{-1}\mathbf{x}) + E_\phi(\rho_i,\phi_i)\mathsf{M}_\phi\mathbf{E}_s(\mathsf{M}_\phi^{-1}\mathbf{x})]e^{i\mathbf{k}_i\cdot\mathbf{b}}\frac{\rho_i d\rho_i d\phi_i}{\cos\theta_i}. \tag{19}$$

C. Collecting the total field by a lens

Now we calculate the effect of the condenser lens on the total field (19). For the backscattered field, the lens L_1 is the condenser, and we assume that it simply maps the field distribution on the sphere of radius f_1 centered on the back principal plane $z=z_1$ (Fig. 2) of the lens L_1 according to Eq. (4),

$$\mathbf{E}(x,y,z_1) = (-\mathbf{e}_\rho\mathbf{e}_\theta\cdot + \mathbf{e}_\phi\mathbf{e}_\phi)\mathbf{E}_{s,\mathrm{tot}}(x,y,-\sqrt{f_1^2-x^2-y^2}). \tag{20}$$

For the field ahead of the probe, both the incident and scattered field are collected by the condenser lens L_2. This yields

$$\mathbf{E}(x,y,z_2) = (\mathbf{e}_\rho\mathbf{e}_\theta\cdot + \mathbf{e}_\phi\mathbf{e}_\phi)\mathbf{E}_{s,\mathrm{tot}}(x,y,\sqrt{f_2^2-x^2-y^2}) - m^{-1/2}\mathbf{E}_i(-mx,-my,z_1), \tag{21}$$

where f_2 is the focal length of the condenser L_2 and $m=f_2/f_1$ is the magnification factor.

D. Response of the position detector

The intensity received by the detector, placed in a plane conjugated to the backfocal plane of L_1, is given by

$$I(x,y) = \begin{cases} \frac{\epsilon_0 c}{2}|\mathbf{E}(x,y,z_1)|^2 & x^2+y^2 < (NAR/n_m)^2 \\ 0 & x^2+y^2 > (NAR/n_m)^2 \end{cases}, \tag{22}$$

where ϵ_0 and c are, respectively, the dielectric permittivity and speed of light in vacuum. NA is the numerical aperture of the detection system, which needs not be the same as NA_1. The response of a PSD is given by the first moments of the intensity distribution

$$\begin{bmatrix} \mathrm{PSD}_x(\mathbf{b}) \\ \mathrm{PSD}_y(\mathbf{b}) \\ \mathrm{PSD}_z(\mathbf{b}) \end{bmatrix} = \begin{bmatrix} \iint xI(x,y)dxdy \\ \iint yI(x,y)dxdy \\ \iint I(x,y)dxdy \end{bmatrix}. \tag{23}$$

The response of a QPD is given by

$$\begin{bmatrix} \mathrm{QPD}_x(\mathbf{b}) \\ \mathrm{QPD}_y(\mathbf{b}) \\ \mathrm{QPD}_z(\mathbf{b}) \end{bmatrix} = \begin{bmatrix} \iint_{x>0} I(x,y)dxdy - \iint_{x<0} I(x,y)dxdy \\ \iint_{y>0} I(x,y)dxdy - \iint_{y<0} I(x,y)dxdy \\ \iint I(x,y)dxdy \end{bmatrix}. \tag{24}$$

Note that in both cases, the axial component of the position vector is deduced from the total intensity that reaches the photodetector. In the case of the BS detection, this is related to interference fringes generated by various backscattered spherical harmonics. The analysis of the total intensity as a means to measure the axial component of the position vector was demonstrated both for FS (theoretically and experimentally) and BS (Ref. 30) detection. We therefore focus our attention on the probe displacements within the focal plane of L_1. In the case of the FS measurement of b_z, the role of the Gouy phase shift was emphasized in Ref. 13.

III. NUMERICAL RESULTS

Figures 3–13 summarize the numerical simulations. We have computed the electromagnetic field for a spherical probe with index of refraction $n_p=1.55$ and radius a ranging in size from 100 to 2000 nm. The probe is immersed into water ($n_m=1.33$). In all simulations we assume an aperture $R=5$ mm for both the lenses L_1 and L_2 and a linearly polarized incident electric field of the form

$$\mathbf{E}_i = e^{-(x_i^2+y_i^2)/w_0^2}\mathbf{e}_x = e^{-\rho_i^2/w_0^2}(\cos\phi_i\,\mathbf{e}_\rho + \sin\phi\,\mathbf{e}_\phi), \tag{25}$$

where the beam waist w_0 is chosen to be equal to R. Finally, we use $\lambda_0=1064$ nm. These values are typical for optical trapping experiments. In each simulation, we calculated the Mie scattering coefficients a_n and b_n (see Appendix A) up to $n=100$ and truncated subsequently the Mie expansions of $\mathbf{E_s}$, keeping only the significant terms.

We use the same incident field for all simulations. We vary the NA only in the plane of the detector. This corresponds to placing an iris between the lens L_1 and the detector plane, which can be done this without changing the incoming beam.

The general picture obtained from the numerical simulations is qualitatively the same with PSD and QPD; most of the numerical results presented later, therefore, concern the PSD detector.

A. Forward- versus backward-scattering detection

In Fig. 3, we plot PSD_x as a function of b_x with $b_y=b_z=0$ for the FS and BS detection schemes. The qualitative observations reported in Ref. 31 are confirmed: with the BS field, the slope changes its sign with the probe size between $a=400$ nm and $a=600$ nm. However, our calculations show also that such a change of sign occurs again between $a=600$ nm and $a=2000$ nm. For the sizes ranging in between these two values, an almost vanishing position sensitivity was found, for example, for $a=1000$ nm. Varying the probe size (see later in Sec. III C), we observed that the PSD response changes its sign many times in the range 100 nm $<a<2000$ nm.

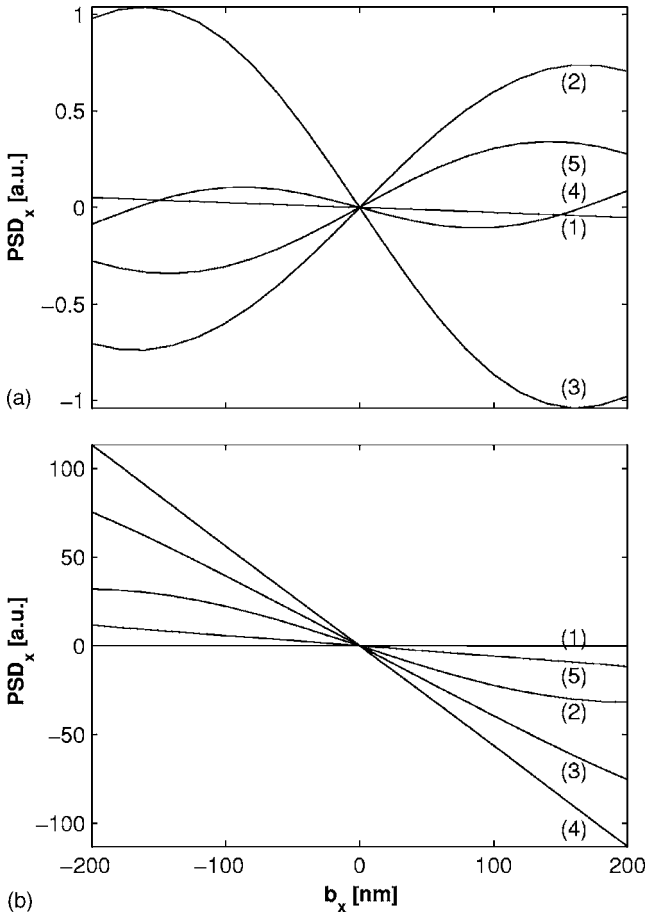

FIG. 3. The response of the PSD as a function of the probe position b_x using the BS (a) and FS (b) fields for different sizes of the probe: $a=200$ (1), 400 (2), 600 (3), 1000 (4), and 2000 nm (5). The probe is illuminated by an x-polarized Gaussian beam focused through a 1.30 NA water immersion objective. The numerical aperture of the detection objective is set to 1.20 both for the BS and FS cases. All curves are normalized to the maximum of PSD_x for $a=600$ nm in the BS detection.

On the other hand, in the FS configuration, the position sensitivity has always the same sign for any probe size. Moreover, the detection signal is about 100 times smaller for the BS detection than with the FS field. Indeed, the BS intensity is much lower than the FS intensity; this can be qualitatively understood from the fact that the reflectivity of a planar interface between the two media is only $(n_p-n_m)^2/(n_p+n_m)^2\approx 1\%$. Finally, the linear detection range is markedly larger with the FS configuration than with the BS configuration.

The cause of these differences may be understood from the field distributions in Figs. 4 and 5. While the FS field essentially has a single-lobe angular intensity distribution for all probe sizes, the BS field distribution becomes more and more complex as a increases. Comparing the results obtained with $a=400$ nm and $a=600$ nm we see that the sign of the response sensitivity changes. While the 400 nm probe results in a spot of a nearly Gaussian shape that moves to the right for $b_x>0$ and to the left for $b_x<0$, the intensity pattern produced by the 600 nm probe moves in the opposite direction.

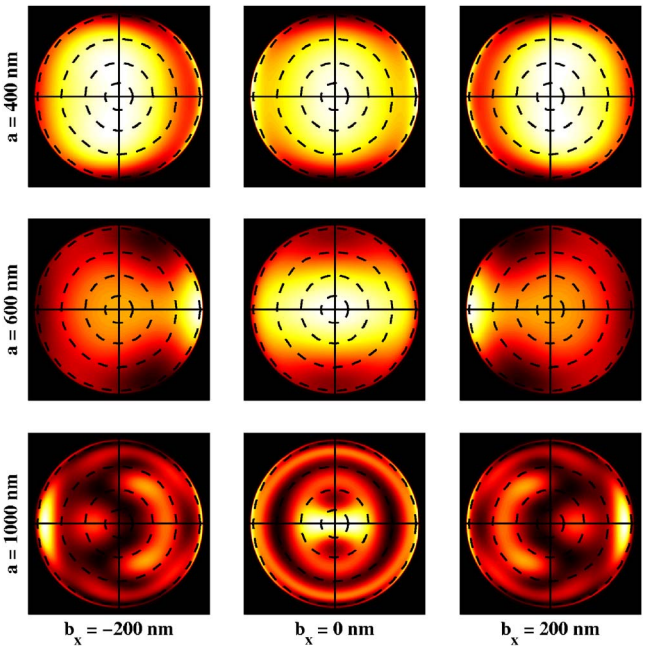

FIG. 4. (Color online) Images of the BS field at the backfocal plane of L_1 for different probe sizes. The dotted circles delimit the areas of the field that is captured by the condenser lens with NA=0.2, 0.5, 0.85, and 1.2, from center outwards.

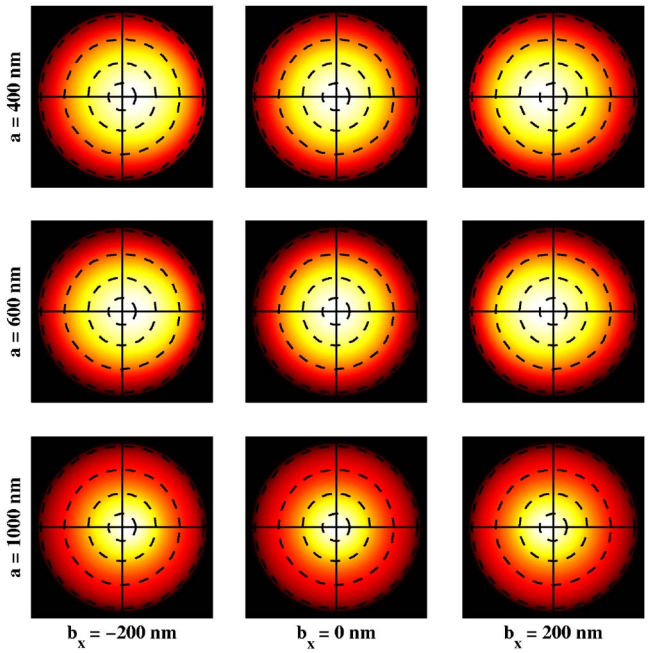

FIG. 5. (Color online) Images of the FS field at the backfocal plane of L_2 for the same parameters as in Fig. 4.

On the other hand, as the 1000 nm probe moves in the x direction, both sides of the detector receive almost the same intensity from the two-lobe BS intensity distribution. This explains the loss of sensitivity for that probe size.

B. Cross talk, numerical aperture, and polarization

The use of the BS field to monitor the position of a probe in both x and y directions requires special care. Indeed, as Figs. 6–9 demonstrate, there is significant cross talk between the x- and y-detection channel. In these figures, we illustrate the detector outputs $\mathrm{PSD}_x(b_x,b_y)$ and $\mathrm{PSD}_y(b_x,b_y)$ for various values of b_y and b_x, respectively, and for NA=1.2, 0.85, 0.5, and 0.2.

In the first column of Fig. 6, we superimpose the $\mathrm{PSD}_x(b_x,b_y=\mathrm{const})$ detection curves for various values of b_y. The curves do not coincide due to the presence of the cross talk between PSD_x and PSD_y. A more detailed picture is given in the second column, which shows contours plots of PSD_x for $b_z=0$ and variable b_x, b_y. The third and fourth column similarly characterize the PSD_y response for NA=1.2.

The difficulties inherent to the use of the BS field can be demonstrated clearly by the results obtained with a

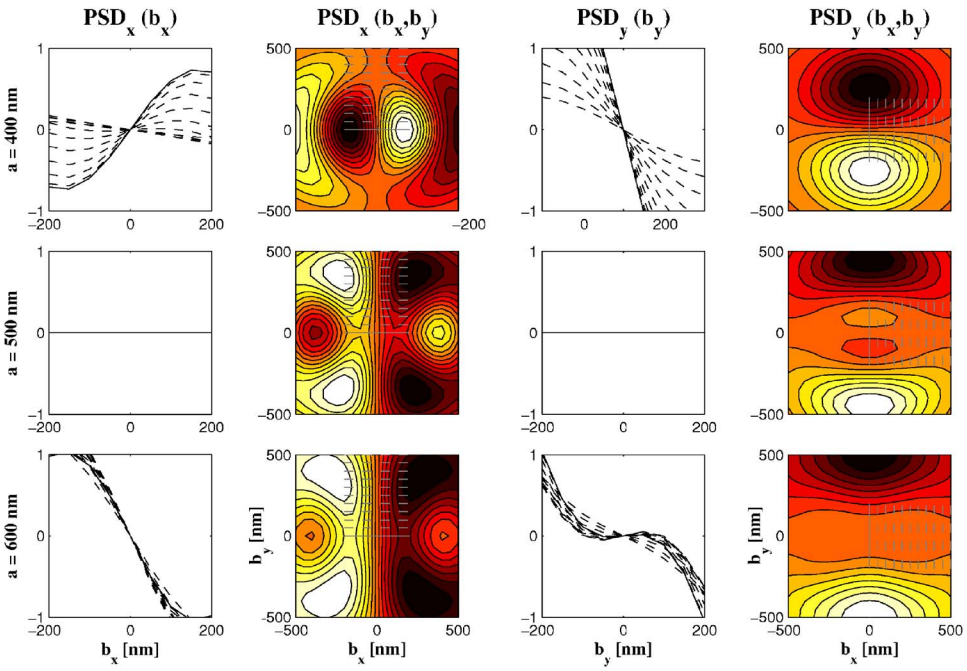

FIG. 6. (Color online) PSD_x (left) and PSD_y (right) for $b_z=0$ and NA=1.2 for various particle sizes. First column: PSD_x for variable b_x and several values of b_y. Second column: contour lines of PSD_x. The color code is normalized independently for each figure for maximum contrast. Third column: PSD_y for variable b_y and several values of b_x. Fourth column: contour lines of PSD_y.

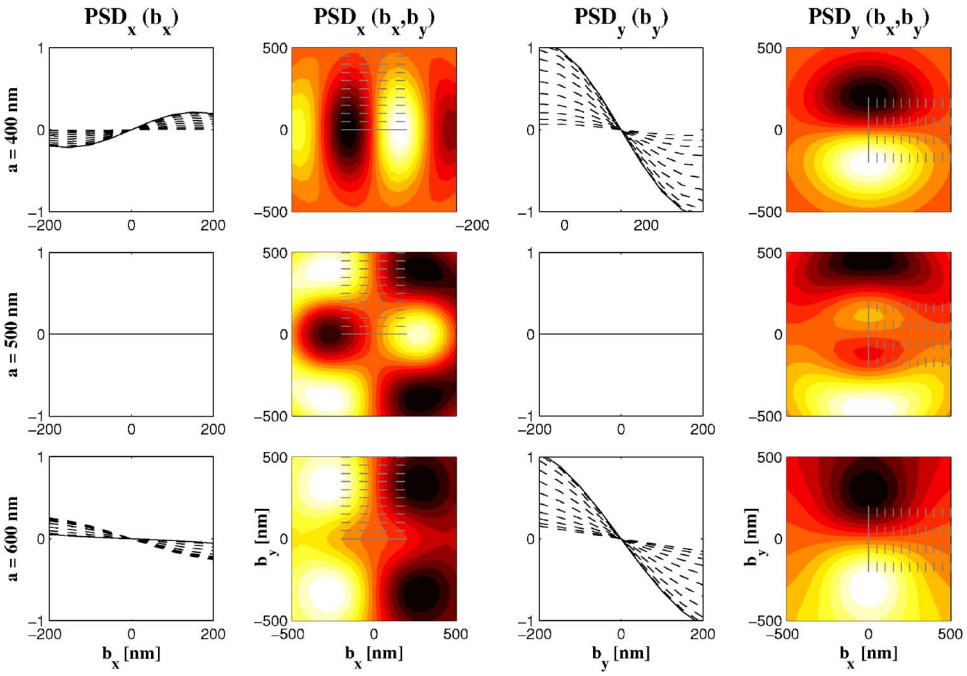

FIG. 7. (Color online) Same as Fig. 6 but with NA=0.85.

=400 nm and NA=1.2: the PSD response curve obtained by the probe motion in the x direction changes the sign of its slope as b_y is varied. In other words, the $\mathrm{PSD}_x(b_x,b_y)$ signal with $b_y \neq 0$ can be opposite to that obtained with $b_y=0$. The cross talk is also present in the FS detection[13] but it is not so strong as in the BS detection.

Comparing next the PSD_x signal for $a=600$ nm and NA=1.2, 0.2, we observe that the numerical aperture of the detection system can similarly alter the response of the detector. This is again to be attributed to the multilobed intensity distribution of the BS field. Note that the effect of NA on the FS detection was discussed in Ref. 39.

The detection beam with polarization perpendicular to the direction of the probe displacement provides higher sensitivity than the beam with parallel polarization. Indeed, for all the NA values studied and $a=400$ nm, Figs. 6–9 show that the values of the PSD_y signal greatly surpasses those of the PSD_x signal.

C. Dependence of the detection sensitivity on probe size

Figures 10 and 11 summarize the influence of the probe size on the detection efficiency. Figure 10 depicts $\mathrm{PSD}_x(b_x,0,0)$ with a as a variable. We find that the detector response undergoes a modulation as a varies. Similarly, Fig. 11 depicts $\mathrm{PSD}_y(0,b_y,0)$ for different a.

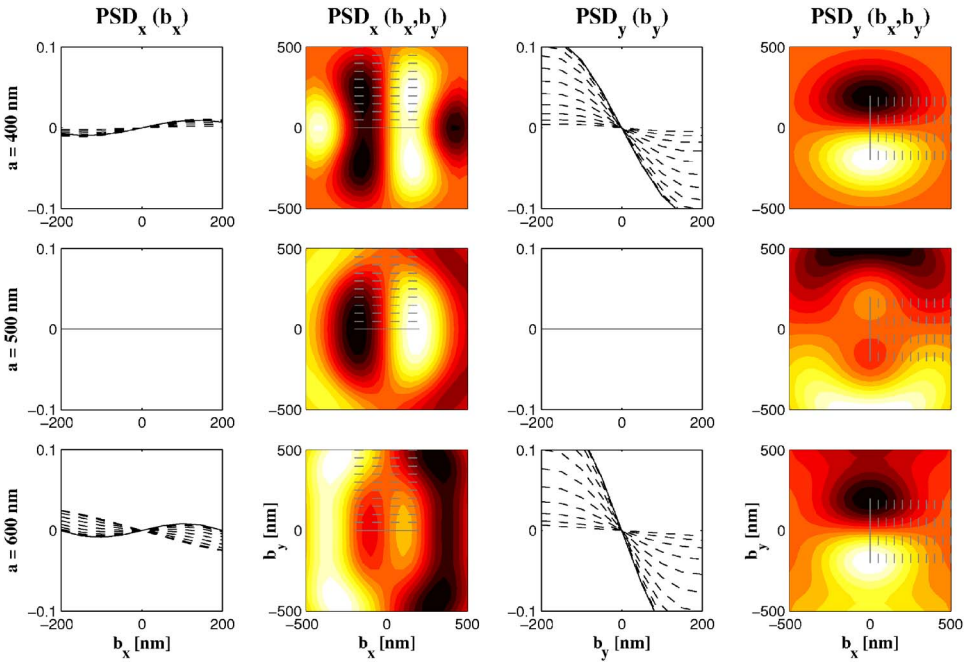

FIG. 8. (Color online) Same as Fig. 6 but with NA=0.5.

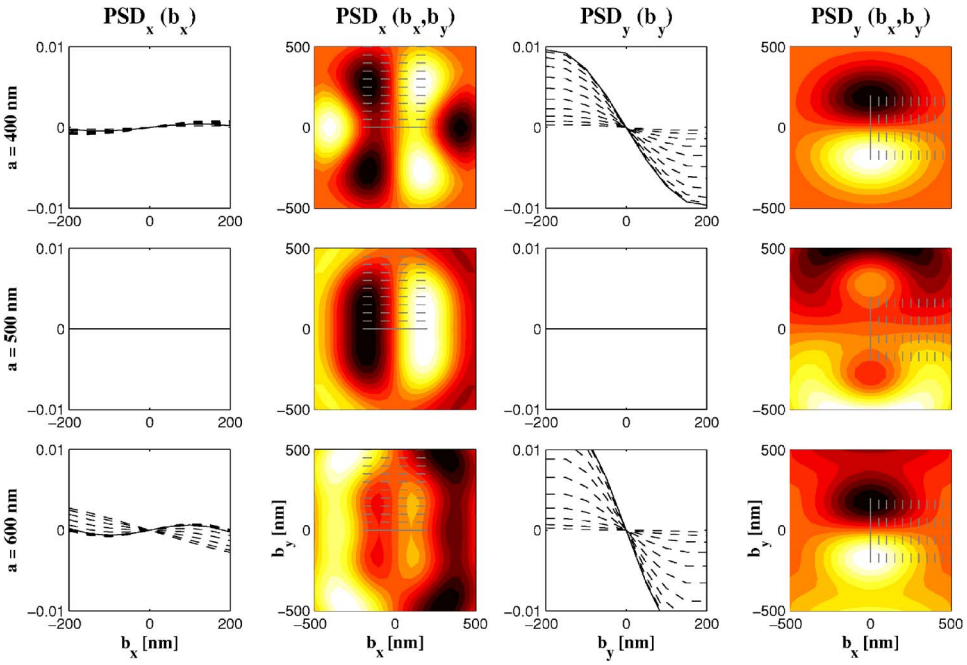

FIG. 9. (Color online) Same as Fig. 6 but with NA=0.2.

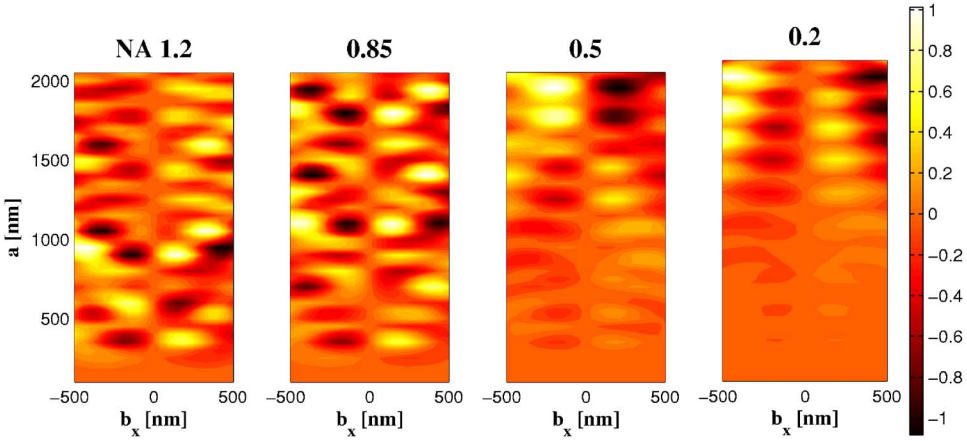

FIG. 10. (Color online) PSD_x as a function of b_x and probe size a for $b_y = b_z = 0$.

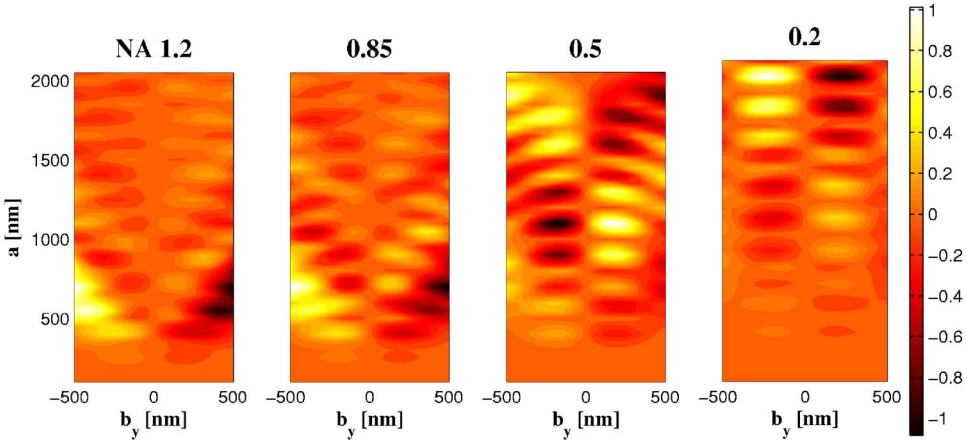

FIG. 11. (Color online) PSD_y as a function of b_y and probe size a for $b_x = b_z = 0$.

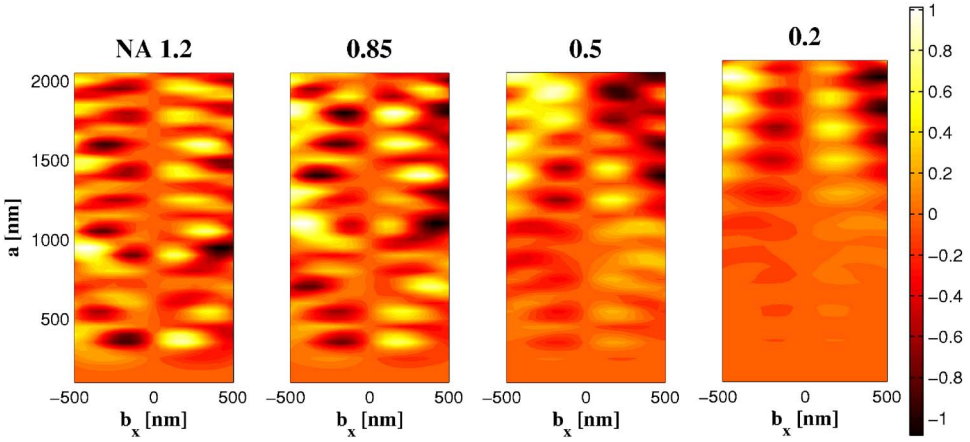

FIG. 12. (Color online) QPD_x as a function of b_x and probe size a for $b_y = b_z = 0$.

Comparing Figs. 10 and 11 for NA=0.2 and $a > 1000$ nm, one can see that the linear detection range is larger for PSD_y than for PSD_x.

There is a minimum of sensitivity for both PSD_x and PSD_y for $a \approx 1000$ nm followed by other minima as a increases by approximately 125 nm. Moreover, considering, for instance, Fig. 11 with NA=0.5, we note that the sensitivity vanishes around $a=800$ nm and $a=1500$ nm.

Finally, we observe that the PSD response is more regular for small NA values. In these cases, indeed, the number of intensity lobes captured by the detector is reduced compared to high NA values. Reducing the numerical aperture, however, implies diminishing the intensity collected by the detectors.

Most of the features reported earlier can be attributed to the complex radiation pattern for the BS comparing to the FS. This radiation pattern changes qualitatively as a increases, which can be traced back to classical Mie scattering.[38] Indeed, with the increase of a, more and more vector spherical harmonics are significant in the radiation pattern. Moreover, successive spherical harmonics have a backscattering radiation pattern that alternately has a zero of intensity and a maximum of intensity for $\theta = \pi$. The same is expected to happen to some extent to the total BS field, which correlates with the modulation of the position sensitivity of the detector. In fact, when computing the FS field for larger probe sizes, we found that the position sensitivity can also change its sign, corresponding again to a transition to multilobed intensity patterns. This occurs, however, for larger probe sizes than those usually used in optical trapping experiments.

D. Comparison of PSD and QPD

The comparison of the response for the two detection methods considered, namely the PSD (Figs. 10 and 11) and the QPD (Figs. 12 and 13), does not show a deep qualitative difference. In particular, we do not find a clear advantage of using the PS-based detection over the QPD-based detection. This does not necessarily contradict the experimental findings of Ref. 31, as the differences reported there were only obtained for a single probe size. Furthermore, spherical aberrations caused by an oil-immersion objective as well as optical forces exerted on the probe should be taken into account because the same beam was used both for trapping and detection.

IV. CONCLUDING REMARKS

Our analysis reveals that the use of BS detection presents a number of difficulties that are absent from the FS detection and this must be taken into account for reliable measurements. Particular attention should be paid to the probe size, as there exist specific sizes for which the probe displacement cannot be detected. Next, the cross talk between the x- and y-detection channels is more significant than by the FS detection and it needs to be carefully com-

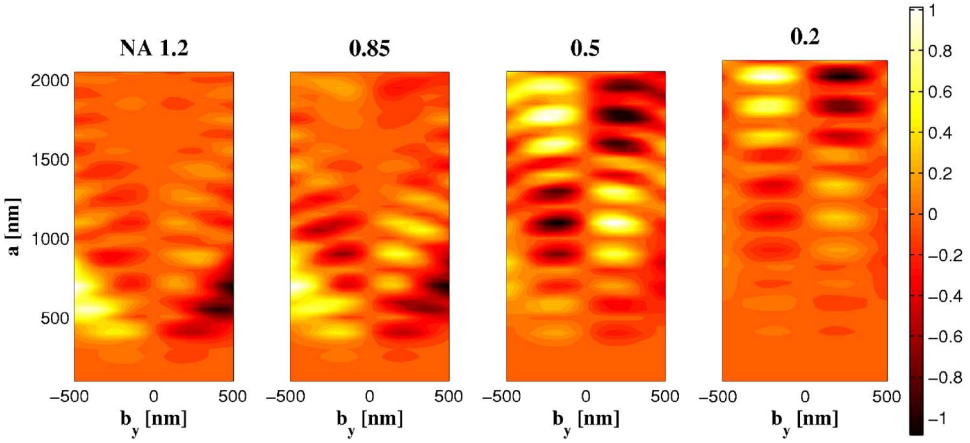

FIG. 13. (Color online) QPD_y as a function of b_y and probe size a for $b_x = b_z = 0$.

pensated for the two-dimensional position monitoring. We also found that the polarization of the detection beam is a useful parameter when information on displacement in one direction only is required. Specifically, the detection beam with the polarization perpendicular to the direction of displacement is preferable.

We showed how the response of the detection system is sensitive to the choice of the numerical aperture of the condenser lens. More specifically, decreasing the numerical aperture produces a more regular detector response as a function of the probe size; however, this reduces the signal intensity.

All the features mentioned earlier are due to the more complex intensity pattern for the BS field than for the FS field. This pattern changes considerably as the radius of the probe increases because the BS field contains more and more vector spherical harmonics.

We studied the situation where trapping and position detection are independent. This requires the detection beam to be sufficiently weak so that it affects negligibly the trapping potential for the probe. However, some experiments require the detection beam to be the same as the trapping beam. In that case, the probe is trapped out of the focal plane due to the scattering force of the beam, i.e., at $z_0 > 0$ in our notation. Now one should consider the optical forces acting on the probe, find out the coordinates of the trapping point, and then perform the study described earlier around this point.

ACKNOWLEDGMENTS

This research was carried out with the financial support of the Spanish Ministry of Education and Science (NAN 2004-09348-C04-02). It was also supported by the Department d'Universitats, Recerca i Societat de la Informacio (Generalitat de Catalunya.) G.K. is a postdoctoral researcher of the Belgian Fonds National de la Recherche Scientifique (F.R.S-FNRS).

APPENDIX A: MIE SCATTERING OF AN *x*-POLARIZED PLANE WAVE

In this appendix, we recall the expressions given in Ref. 38 which we used to compute the Mie-scattering fields. Given an x-polarized plane incoming wave

$$\mathbf{E_i} = e^{ikz}\mathbf{e_x}, \tag{A1}$$

the expression for the scattered field is

$$\mathbf{E_s} = \sum_{n=1}^{+\infty} E_n[ia_n\mathbf{N}_{e1n}^{(3)} - b_n\mathbf{M}_{o1n}^{(3)}], \tag{A2}$$

where

$$E_n = i^n\frac{2n+1}{n(n+1)}, \tag{A3}$$

a_n and b_n are the scattering coefficients and $\mathbf{N}_{e1n}^{(3)}$ and $\mathbf{M}_{o1n}^{3}$ are vector spherical harmonics (with $m=1$). These are given by

$$\mathbf{N}_{e1n}^{(3)} = \cos\phi\, n(n+1)\sin\theta\, \pi_n(\cos\theta)\frac{h_n^{(1)}(\varrho)}{\varrho}\mathbf{e_r} + \cos\phi\, \tau_n(\cos\theta)\frac{\frac{d}{d\varrho}[\varrho h_n^{(1)}(\varrho)]}{\varrho}\mathbf{e}_\theta - \sin\phi\, \pi_n(\cos\theta)\frac{\frac{d}{d\varrho}[\varrho h_n^{(1)}(\varrho)]}{\varrho}\mathbf{e}_\phi, \tag{A4}$$

$$\mathbf{M}_{o1n}^{(3)} = \cos\phi\, \pi_n(\cos\theta)h_n^{(1)}(\varrho)\mathbf{e}_\theta - \sin\phi\, \tau_n(\cos\theta)h_n^{(1)}(\varrho)\mathbf{e}_\phi, \tag{A5}$$

where

$$\varrho = kr,$$

$$h_n^{(1)}(\varrho) = j_n(\varrho) + iy_n(\varrho) = \sqrt{\frac{\pi}{2\varrho}}J_{n+1/2}(\varrho) + i\sqrt{\frac{\pi}{2\varrho}}Y_{n+1/2}(\varrho),$$

with $h_n^{(1)}$ as a spherical Bessel function of the third kind or spherical Hankel function, j_n and y_n as spherical Bessel functions of the first and second kind, and $J_{n+1/2}$ and $Y_{n+1/2}$ as Bessel functions of the first and second kind. The functions $\pi_n(u)$ and $\tau_n(u)$ can be efficiently computed by upward recurrence from the following relations:

$$\pi_0(u) = 0,$$

$$\pi_1(u) = 1,$$

$$\pi_n(u) = \frac{2n-1}{n-1}u\pi_{n-1}(u) - \frac{n}{n-1}\pi_{n-2}(u),$$

$$\tau_m(u) = nu\pi_n(u) - (n+1)\pi_{n-1}(u).$$

On the other hand, the scattering coefficients come from the boundary conditions and, when the permeability of the probe and the surrounding medium are the same, can be expressed as

$$a_n = \frac{m\psi_n(mx)\psi_n'(x) - m\psi_n(x)\psi_n'(mx)}{m\psi_n(mx)\xi_n'(x) - \xi_n(x)\psi_n'(mx)}, \tag{A6}$$

$$b_n = \frac{\psi_n(mx)\psi_n' - m\psi_n(x)\psi_n'(mx)}{\psi_n(mx)\xi_n'(x) - m\xi_n(x)\psi_n'(mx)}, \tag{A7}$$

where

$$x = ka = \frac{2\pi n_m a}{\lambda},$$

$$m = \frac{k_p}{k_m} = \frac{n_p}{n_m},$$

$$\psi_n(\varrho) = \varrho j_n(\varrho),$$

$$\xi_n(\varrho) = \varrho h_n^{(1)}(\varrho),$$

where n_m is the refractive index of the medium, n_p is the refractive index of the probe, and ψ_n and ξ_n are the Riccati–Bessel functions.

APPENDIX B: ROTATION MATRICES M_ρ AND M_Φ

We now construct the transformation matrices in Eq. (12). Let us consider an arbitrary vector (position, electric field) having the following representations in the coordinate systems of interest:

$$\begin{aligned} x\mathbf{e}_x + y\mathbf{e}_y + z\mathbf{e}_z &= x'\mathbf{e}_{x'} + y'\mathbf{e}_{y'} + z'\mathbf{e}_{z'} \\ &= x''\mathbf{e}_{x''} + y''\mathbf{e}_{y''} + z''\mathbf{e}_{z''} \\ &= x_\rho\mathbf{e}_\rho + x_\phi\mathbf{e}_\phi + x_z\mathbf{e}_z. \end{aligned} \tag{B1}$$

From Eqs. (2) and (3), we have

$$\begin{pmatrix} x \\ y \\ z \end{pmatrix} = \begin{pmatrix} \cos\phi_i & -\sin\phi_i & 0 \\ \sin\phi_i & \cos\phi_i & 0 \\ 0 & 0 & 1 \end{pmatrix} \begin{pmatrix} x_\rho \\ x_\phi \\ x_z \end{pmatrix} \equiv R(\phi_i) \begin{pmatrix} x_\rho \\ x_\phi \\ x_z \end{pmatrix}.$$

On the other hand, from Eqs. (5) and (6), the relation between (x',y',z') and (x_ρ,x_ϕ,x_z) is

$$\begin{pmatrix} x_\rho \\ x_\phi \\ x_z \end{pmatrix} = \begin{pmatrix} \cos\theta_i & 0 & -\sin\theta_i \\ 0 & 1 & 0 \\ \sin\theta_i & 0 & \cos\theta_i \end{pmatrix} \begin{pmatrix} x' \\ y' \\ z' \end{pmatrix} = L(\theta_i) \begin{pmatrix} x' \\ y' \\ z' \end{pmatrix}.$$

Hence, $\mathsf{M}_\rho = R(\phi_i)L(\theta_i)$. Next, we have

$$\begin{pmatrix} x' \\ y' \\ z' \end{pmatrix} = \begin{pmatrix} 0 & -1 & 0 \\ 1 & 0 & 0 \\ 0 & 0 & 1 \end{pmatrix} \begin{pmatrix} x'' \\ y'' \\ z'' \end{pmatrix} = R\left(\frac{\pi}{2}\right) \begin{pmatrix} x'' \\ y'' \\ z'' \end{pmatrix},$$

giving $\mathsf{M}_\phi = R(\phi_i)L(\theta_i)R(\pi/2)$.

The scattered field $\Sigma_i E_{s,i}(\mathbf{x}')\mathbf{e}_i'$ in the rotated system $(\mathbf{e}_{x'},\mathbf{e}_{y'},\mathbf{e}_{z'})$ system is given by $\Sigma_i F_{s,i}(\mathbf{x})\mathbf{e}_i$ in the unrotated frame, where

$$\begin{bmatrix} F_x(\mathbf{x}) \\ F_y(\mathbf{x}) \\ F_z(\mathbf{x}) \end{bmatrix} = \mathsf{M}_\rho \begin{bmatrix} E_{s1}(\mathbf{x}') \\ E_{s2}(\mathbf{x}') \\ E_{s3}(\mathbf{x}') \end{bmatrix},$$

$$\begin{pmatrix} x' \\ y' \\ z' \end{pmatrix} = \mathsf{M}_\rho^{-1} \begin{pmatrix} x \\ y \\ z \end{pmatrix}.$$

[1] L. P. Ghislain and W. W. Webb, Opt. Lett. **18**, 1678 (1993).
[2] L. P. Ghislain, N. A. Switz, and W. W. Webb, Rev. Sci. Instrum. **65**, 2762 (1994).
[3] K. Svoboda, C. F. Schmidt, B. J. Schnapp, and S. M. Block, Nature (London) **365**, 721 (1993).
[4] A. D. Mehta, M. Rief, J. A. Spudich, D. A. Smith, and R. M. Simmons, Science **283**, 1689 (1999).
[5] D. E. Smith, S. J. Tans, S. B. Smith, S. Grimes, D. L. Anderson, and C. Bustamante, Nature (London) **413**, 748 (2001).
[6] J.-D. Wen, M. Manosas, P. T. X. Li, S. B. Smith, C. Bustamante, F. Ritort, and I. Tinoco, Biophys. J. **92**, 2996 (2007).
[7] W. Denk and W. W. Webb, Appl. Opt. **29**, 2382 (1990).
[8] F. Gittes and C. F. Schmidt, Opt. Lett. **23**, 7 (1998).
[9] A. Pralle, M. Prummer, E.-L. Florin, E. H. K. Stelzer, and J. K. H. Hörber, Microsc. Res. Tech. **44**, 378 (1999).
[10] K. Berg-Sørensen and H. Flyvbjerg, Rev. Sci. Instrum. **75**, 594 (2004).
[11] K. Visscher and S. M. Block, Methods Enzymol. **298**, 460 (1998).
[12] S. F. Tolić-Nørrelykke, E. Schäffer, J. Howard, F. Pavone, F. Jülicher, and H. Flyvbjerg, Rev. Sci. Instrum. **77**, 103101 (2006).
[13] A. Rohrbach and E. H. K. Stelzer, J. Appl. Phys. **91**, 5474 (2002).
[14] S. B. Smith, Y. Cui, and C. Bustamante, Methods Enzymol. **361**, 134 (2003).
[15] M. J. Lang, C. L. Asbury, J. W. Shaevitz, and S. M. Block, Biophys. J. **83**, 491 (2002).
[16] I. M. Peters, B. G. de Grooth, J. M. Schins, C. G. Figdor, and J. Greve, Rev. Sci. Instrum. **69**, 2762 (1998).
[17] K. C. Vermeulen, J. van Mameren, G. J. M. Stienen, E. J. G. Peterman, G. J. L. Wuite, and C. F. Schmidt, Rev. Sci. Instrum. **77**, 013704 (2006).
[18] M. W. Allersma, F. Gittes, M. J. deCastro, R. J. Stewart, and C. F. Schmidt, Biophys. J. **74**, 1074 (1998).
[19] D. M. Carberry, J. C. Reid, G. M. Wang, E. M. Sevick, D. J. Searles, and D. J. Evans, Phys. Rev. Lett. **92**, 140601 (2004).
[20] A. R. Clapp, A. G. Ruta, and R. B. Dickinson, Rev. Sci. Instrum. **70**, 2627 (1999).
[21] J. W. Shaevitz, E. A. Abbondanzieri, R. Landick, and S. M. Steven, Nature (London) **426**, 684 (2003).
[22] J. R. Moffitt, Y. R. Chemla, D. Izhaky, and C. Bustamante, Proc. Natl. Acad. Sci. U.S.A. **103**, 9006 (2006).
[23] G. Volpe and D. Petrov, Phys. Rev. Lett. **97**, 210603 (2006).
[24] A. Ashkin, K. Schütze, J. M. Dziedzic, U. Euteneuer, and M. Schliwa, Nature (London) **348**, 346 (1990).
[25] S. Block, L. S. B. Goldstein, and B. J. Schnapp, Nature (London) **348**, 348 (1990).
[26] J. Dapprich and N. Nicklaus, Bioimaging **6**, 25 (1998).
[27] M. E. J. Friese, A. G. Truscott, H. Rubinsztein-Dunlop, and N. R. Heckenberg, Appl. Opt. **38**, 6597 (1999).
[28] G. Volpe, R. Quidant, G. Badenes, and D. Petrov, Phys. Rev. Lett. **96**, 238101 (2006).
[29] M. R. J. Friese, H. Rubinsztein-Dunlop, N. R. Heckenberg, and E. W. Dearden, Appl. Opt. **35**, 7112 (1996).
[30] W. Singer, S. Bernet, N. Hecker, and M. Ritsch-Marte, J. Mod. Opt. **47**, 2921 (2000).
[31] J. H. G. Huisstede, K. O. van der Werf, M. L. Bennink, and V. Subramaniam, Opt. Express **13**, 1113 (2005).
[32] A. Jonas, P. Zemanek, and E. L. Florin, Opt. Lett. **26**, 1466 (2001).
[33] B. Ovryn and S. H. Izen, J. Opt. Soc. Am. A **17**, 1202 (2000).
[34] P. Török, P. D. Higdon, R. Juškaitis, and T. Wilson, Opt. Commun. **155**, 335 (1998).
[35] M. Leutenegger, R. Rao, R. A. Leitgeb, and T. Lasser, Opt. Express **14**, 11277 (2006).
[36] M. Born and E. Wolf, *Principles of Optics: Electromagnetic Theory of Propagation, Interference and Diffraction of Light* (Cambridge University Press, Cambridge, 1997).
[37] E. Wolf, Proc. R. Soc. London, Ser. A **253**, 349 (1959).
[38] C. F. Bohren and D. R. Huffman, *Absorption and Scattering of Light by Small Particles* (Wiley, New York, 1983).
[39] A. Rohrbach, H. Kress, and E. H. K. Stelzer, Opt. Lett. **28**, 411 (2003).